Available online at www.sciencedirect.com
SCIENCE DIRECT®
Journal of Computational Physics 206 (2005) 536–558
JOURNAL OF COMPUTATIONAL PHYSICS
www.elsevier.com/locate/jcp

Accurate three-dimensional lid-driven cavity flow

S. Albensoeder *, H.C. Kuhlmann

Institute of Fluid Mechanics and Heat Transfer, Vienna University of Technology, Resselgasse 3/1/2, A-1040 Vienna, Austria

Received 29 June 2004; received in revised form 24 December 2004; accepted 24 December 2004
Available online 22 February 2005

Abstract

A Chebyshev-collocation method in space is introduced, which allows an accurate calculation of three-dimensional lid-driven cavity flows. The time integration is carried out by an Adams–Bashforth backward–Euler scheme. The accuracy of the method relies on the representation of the solution as a superposition of stationary local asymptotic solutions and a residual flow field. This way the most severe discontinuities in the boundary conditions, which arise along the lines where moving and stationary walls meet, are taken care of analytically and thus do not spoil the numerical part of the solution. Calculations are carried out for no-slip boundary conditions at the cavity end-walls as well as for periodic end-wall conditions. In general, the spatial accuracy is better than fifth order. For rigid end-wall conditions, the accuracy is reduced near the end-walls to $\mathcal{O}(N^{3/2})$, but recovers in the bulk. Tabulated data are provided for the most interesting flow properties.

1. Introduction

The lid-driven-cavity problem is one of the most important benchmarks for numerical Navier–Stokes solvers. Its importance results from the fundamental rectangular or square geometry and the simple driving of the flow by means of the tangential motion with constant velocity of a single lid, representing Dirichlet boundary conditions. Moreover, the driven-cavity flow exhibits a number of interesting physical features. The Prandtl–Batchelor theorem is easily demonstrated as the primary vortex, driven by the wall motion, develops a core of constant vorticity as the Reynolds number is increased (see, e.g. [10]). In addition, flow separation from the stationary wall and the existence of an infinite sequence of viscous corner eddies in the rigid 90°-corners can be observed [35]. The system also exhibits a particular singularity in the boundary conditions where moving and stationary walls meet [47,24,27]. Last but not least, the flow in an infinitely

* Corresponding author. Tel.: +43 1 58801 32211.
E-mail address: salben@fluid.tuwien.ac.at (S. Albensoeder).

0021-9991/$ - see front matter © 2005 Elsevier Inc. All rights reserved.
doi:10.1016/j.jcp.2004.12.024

extended system undergoes a sequence of instabilities and transitions when the speed of the lid is increased before becoming turbulent. The particular scenario depends very much on the aspect ratio of the cavity. A recent review on the flow physics in the driven cavity was given by Shankar and Deshpande [42].

Ghia et al. [19] and Schreiber and Keller [40] were among the first to publish benchmark data on the lid-driven cavity flow. These classical papers are frequently referenced even today. At about the same time, the interest in the flow physics of interior recirculating flows was revived, after the pioneering works of Burggraf [10] and Pan and Acrivos [36]. The renewed interest led to a series of papers by Koeseff et al. [31], Freitas et al. [18], and coworkers, focussing on the three-dimensional vortical structures and on end-wall effects.

During the course of time the grid resolution and the numerical accuracy were significantly improved and even more accurate solutions of the two-dimensional problem have been calculated. Highly accurate two-dimensional solutions have been obtained by Botella and Peyret [8] using a spectral method in which the effect of the corner discontinuity on the numerical solution was reduced by the incorporation of an asymptotic solution for the flow in the direct vicinity of the singular corners. For an efficient elimination of the singularity, they made use of the leading-order Stokes flow [35] plus the first-order nonlinear correction (see, e.g. [24]). A similar procedure, merely taking into account the leading-order Stokes-flow solution, was previously introduced by Schultz et al. [41].

Since two-dimensional, time-dependent calculations are significantly less costly than full three-dimensional simulations, the Hopf bifurcation at high Reynolds numbers of the pure two-dimensional flow was investigated with high precision by Goodrich et al. [22], Shen [44], Abouhamza and Pierre [1], and Auteri et al. [3,4]. While these calculation are of fundamental interest for benchmarking, they are less relevant for real flows. The oscillatory two-dimensional flows exist only for such high Reynolds numbers $Re = O(10^4)$ that they are very unlikely to be observed experimentally. Albensoeder et al. [2] have shown that the two-dimensional steady flow becomes unstable to genuinely three-dimensional flows at Reynolds numbers one order of magnitude smaller than those at which the two-dimensional flow oscillations have been computed.

Some of the first three-dimensional cavity-flow calculations were carried out by De Vahl Davis and Mallinson [14] and Goda [20]. The relevance of three-dimensional flows in general was demonstrated by Freitas et al. [18]. In particular, three-dimensional effects near the end-walls of a finite-size system which can be realized in the laboratory were pointed out by Koseff and Street [30]. In order to clarify the observed three-dimensional flow structures numerically, a series of benchmark tests for the lid-driven square cavity was undertaken for a Reynolds number of 3200. The results, however, published in Deville et al. [15], remained inconclusive, because the numerical solutions obtained by different methods and resolutions scattered significantly. An important point in this regard is the fact that end-wall effects in finite-length systems can, to a certain degree, suppress the intrinsic three-dimensional flow instabilities in the bulk of the cavity [2]. During the last years, further three-dimensional calculations have become available, see e.g. Ku et al. [32], Cortes and Miller [13], Babu and Korpela [5], and Wang and Sheu [48]. Further contributions of Iwatsu et al. [29], Chiang et al. [11,12], and Sheu and Tsai [45] primarily focussed on the flow structure and topology, and not on benchmarking.

Until recently, numerical calculations have predominantly be performed for two-dimensional flows. We have, however, carried out the first *correct* three-dimensional linear stability analysis of the two-dimensional cavity flow with periodic boundary conditions in the spanwise direction [2]. The uncertainty of the critical Reynolds number was of the order of magnitude of 1%. Despite the sparseness of reliable stability data, our results were validated by comparison with neutral-stability data of Ding and Kawahara [16,17] and by critical Reynolds numbers of Kuhlmann et al. [33]. Additional confidence was gained from our own experimental results [2] and from the numerical work of Spasov et al. [46] and Shatrov et al. [43]. After having become three-dimensional, the cavity flow develops into a turbulent flow upon a further increase of the Reynolds number. Apart from the work of Leriche and Gavrilakis [34], the turbulent flow regime has not yet been seriously tackled numerically for Reynolds numbers of the order of $Re = O(10^4)$ and above.

During our investigation of the transition to three-dimensional flow the lack of numerical data for nonlinear three-dimensional flows became obvious. Owing to their physical significance and the fact that laminar three-dimensional flows have become accessible by numerical methods, we have carried out a number of systematic calculations in order to provide high-accuracy numerical data for the three-dimensional cavity flow. In the next section, the problem will be formulated. Thereafter, the numerical methods will be described and a validation of the code is performed. Our benchmark results are presented and discussed in Section 5. Finally, a summary of the results is provided in the conclusion.

2. Problem formulation

We consider the flow of a Newtonian fluid with constant viscosity ν and constant density ρ in a rectangular cavity of the size $d \times h \times l$ in x-, y-, and z-direction, respectively. The flow is driven by the wall at $x = -d/2$ which moves tangentially in y-direction with constant velocity V. The geometry is sketched in Fig. 1.

The scales h, ν/h, $\rho\nu^2/h^2$, and h^2/ν are used to non-dimensionalize the length $\mathbf{x} = (x, y, z)$, velocity $\mathbf{u} = (u, v, w)$, pressure p, and time t, respectively. The scaled Navier–Stokes equations then take the form

$$\frac{\partial \mathbf{u}}{\partial t} + \mathbf{u} \cdot \nabla \mathbf{u} = -\nabla p + \nabla^2 \mathbf{u}, \tag{1a}$$

$$\nabla \cdot \mathbf{u} = 0. \tag{1b}$$

The no-slip/no-penetration boundary conditions in the x- and y-directions are:

$$\mathbf{u}(x = -\Gamma/2) = Re\, \mathbf{e}_y, \tag{2a}$$

$$\mathbf{u}(x = \Gamma/2) = 0, \tag{2b}$$

$$\mathbf{u}(y = \pm 1/2) = 0, \tag{2c}$$

where the Reynolds number is defined as

$$Re = \frac{Vh}{\nu}. \tag{3}$$

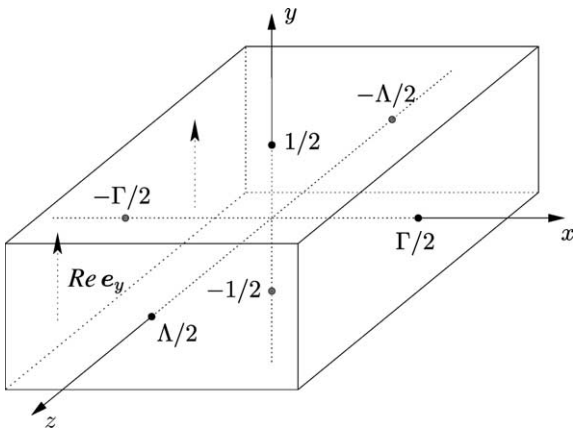

Fig. 1. Geometry of the lid-driven cavity.

The geometry is characterized by two aspect ratios, the cross-sectional aspect ratio

$$\Gamma = \frac{d}{h} \tag{4}$$

and the span aspect ratio

$$\Lambda = \frac{l}{h}, \tag{5}$$

the latter of which defines the extent of the system in z-direction. On the boundaries at $z = \pm\Lambda/2$, we impose either no-slip/no-penetration boundary conditions,

$$\mathbf{u}(z = \pm\Lambda/2) = 0, \tag{6}$$

or periodic boundary conditions

$$\mathbf{u}(z = \Lambda/2) = \mathbf{u}(z = -\Lambda/2) \quad \text{and} \quad p(z = \Lambda/2) = p(z = -\Lambda/2). \tag{7}$$

The no-slip boundary conditions are appropriate for calculations representing a finite container. The periodic boundary conditions, on the other hand, are useful for the computation of flows unperturbed by the sidewalls. These latter boundary conditions are frequently used when bulk flow instabilities are studied. Yet, the periodic boundary conditions limit the maximum modulation length of the three-dimensional pattern to Λ, i.e., the wave-number spectrum in z-direction of the flow structure is bounded from below and long-wavelength modulations are suppressed.

3. Numerical procedure

3.1. Discretization and algorithm

The numerical scheme is an extension to three dimensions of the two-dimensional numerical scheme of Botella and Peyret [8]. The spatial discretization is achieved by using the so-called $\mathscr{P}_N - \mathscr{P}_{N-2}$ collocation method [39,8,37]. In this procedure, the velocities are approximated by polynomials of the order N while the pressure is approximated by polynomials of the order $N-2$. Explicitly, the velocity is represented as

$$\mathbf{u}(\mathbf{x}) = \sum_{i=0}^{N_x} \sum_{j=0}^{N_y} \sum_{k=0}^{N_z} \hat{\mathbf{u}}_{ijk} h_i\left(\frac{2}{\Gamma}x\right) h_j(2y) h_k\left(\frac{2}{\Lambda}z\right), \tag{8}$$

with polynomials h_n of orders N_x, N_y, and N_z in the x-, y-, and z-directions, respectively. The computational nodes are the Gauss–Lobatto points

$$\mathbf{x}_{ijk} = (x_i, y_j, z_k) = \left[\frac{\Gamma}{2}\cos\left(i\frac{\pi}{N_x}\right), \frac{1}{2}\cos\left(j\frac{\pi}{N_y}\right), \frac{\Lambda}{2}\cos\left(k\frac{\pi}{N_z}\right)\right]^{\mathrm{T}}, \tag{9}$$

with $i = 0, \ldots, N_x$, $j = 0, \ldots, N_y$, and $k = 0, \ldots, N_z$. The pressure is approximated by

$$p(\mathbf{x}) = \sum_{i=1}^{N_x-1} \sum_{j=1}^{N_y-1} \sum_{k=1}^{N_z-1} \hat{p}_{ijk} \breve{h}_i\left(\frac{2}{\Gamma}x\right) \breve{h}_j(2y) \breve{h}_k\left(\frac{2}{\Lambda}z\right) \tag{10}$$

using polynomials $\breve{h}_n$ of order less by 2 compared to h_n. This ansatz is used for rigid boundary conditions in z-direction.

For periodic boundary conditions, the polynomials $h_k(2z/\Lambda)$ and $\breve{h}_k(2z/\Lambda)$ in (8) and (10) are replaced by harmonics $\tilde{h}_k(2/\Lambda\, z)$. These harmonics are computed on an equidistant grid such that z_k in (9) must be replaced by

$$z_k = \frac{\Lambda}{2}\left[\frac{2(k-1)}{N_z-1} - 1\right]. \tag{11}$$

Note that the index for the computational nodes in z-direction now runs from $k = 1$ to $k = N_z - 1$. Hence, all functions are represented in Fourier space $\mathscr{F}^{N-2}$ by the Fourier modes $\mathrm{e}^{-\mathrm{i}\pi nz/\Lambda}$ with $n = -(N_z-1)/2, \ldots, (N_z-1)/2-1$. This representation allows an easy change from rigid to periodic boundary conditions in z-direction and vice versa, just by replacing the approximation functions and their derivative matrices. As an advantage of the $\mathscr{P}_N - \mathscr{P}_{N-2}$ method, no boundary conditions for the pressure are required which could possibly produce non-physical spurious modes.

For the time discretization, we use an Adams–Bashforth backward–Euler scheme. This scheme is second-order accurate in time for the velocities and the pressure [7,28]. The efficiency of this method has been demonstrated by Botella [7]. The time-integration scheme splits one time step into a prediction step for the intermediate velocity field $\bar{\mathbf{u}}$

$$\frac{3\bar{\mathbf{u}}^{n+1} - 4\mathbf{u}^n + \mathbf{u}^{n-1}}{2\Delta t} - \Delta\bar{\mathbf{u}}^{n+1} + \nabla p^n + 2\mathbf{u}^n\cdot\nabla\mathbf{u}^n - \mathbf{u}^{n-1}\cdot\nabla\mathbf{u}^{n-1} = \mathbf{f}^{n+1}, \tag{12a}$$

$$\bar{\mathbf{u}}^{n+1}\big|_{\partial V} = \mathbf{g}^{n+1} \tag{12b}$$

and a projection step

$$\frac{3}{2}\frac{\mathbf{u}^{n+1} - \bar{\mathbf{u}}^{n+1}}{\Delta t} + \nabla\left(p^{n+1} - p^n\right) = \mathbf{f}^{n+1}\cdot\mathbf{n}, \tag{13a}$$

$$\nabla\cdot\mathbf{u}^{n+1} = 0, \tag{13b}$$

$$\mathbf{u}^{n+1}\cdot\mathbf{n}\big|_{\partial V} = \mathbf{g}^{n+1}\cdot\mathbf{n}. \tag{13c}$$

Initially, for the first time step ($n = 0$), the velocity and the pressure are set to $\mathbf{u}^{-1} = \mathbf{u}^0$ and $p^0 = 0$, and Δt is replaced by $3\Delta t/2$. These initial conditions reduce (12a)–(13c) to first order. However, the second-order accuracy is preserved for all following time steps.

The equations for the prediction step are solved by a direct Helmholtz solver [25,26]. The solution of the projection step is obtained using the Uzawa method [37] which leads to a Poisson-like equation which is also solved by the direct Helmholtz solver. The constant-pressure mode which leads to a singularity during the solution procedure is filtered using the method of Phillips and Roberts [38].

3.2. Treatment of the edge and corner singularities

Along the edges between the moving and the stationary walls of the cavity the flow fields are singular. On the edges $(x, y) = (-\Gamma/2, \pm 1/2)$ which are perpendicular to the direction of the wall motion both the vorticity and the pressure diverge, whereas on the edges parallel to the direction of the wall motion $(x, z) = (-\Gamma/2, \pm\Lambda/2)$ only the vorticity diverges. These latter singularities only arise for rigid end-wall conditions. The problem is even further complicated by the presence of three-dimensional corners where two singular edges meet.

Such singularities can severely degrade the convergence of any spectral method. As a remedy, one could make use of a function $\mathbf{u}_c$ which is identical to the local asymptotic solutions at all singular edges and corners. If a function $\mathbf{u}_c$ can be constructed such that the residuum $\mathbf{u}_* = \mathbf{u} - \mathbf{u}_c$ is smooth and finite everywhere

on the boundary of the domain, then the problem could be solved very efficiently. In the lid-driven cavity problem, the natural building blocks for the function $\mathbf{u}_c$ are local asymptotic solutions for a single infinite wedge [47,35,24,27] and the three-dimensional local asymptotic solution for the flow in the quadrant of a three-dimensional rectangular corner formed by two stationary walls and one wall sliding parallel to one of the edges [21].

To understand the convergence rate of $\mathbf{u}_*$ in more detail we must consider the error, or residuum, of magnitude $\mathcal{O}(N^{-\gamma})$ for the Chebyshev-spectral method, where N is the number of unknowns and γ a coefficient which is related to the regularity of the solution. Bottela and Peyret [9] have evaluated the exponent γ theoretically and numerically for several test problems, using different norms. For the two-dimensional asymptotic solution $\mathbf{u} = r^{\alpha}\mathbf{f}(\theta)$ for a singular edge, where r and θ are polar-coordinates centered on the edge, they found $\gamma = 2\alpha + 1$ when using a L^2_ω-norm (see Section 5.1). The power α of r of the most singular term determines the convergence of the numerical solution.

Let us first consider the two-dimensional cavity problem ($\Lambda \to \infty$). Then the asymptotic solutions near the four corners $A = (-\Gamma/2, -1/2)$, $B = (-\Gamma/2, 1/2)$, $C = (\Gamma/2, 1/2)$, and $D = (\Gamma/2, -1/2)$ can be written in form of a power series $\mathbf{u}^{(i)} = \sum_{j=1}^{\infty} r^{\alpha_j^{(i)}} \mathbf{f}_j^{(i)}(\theta)$, where $i \in \{A, B, C, D\}$ is the index of the corner. It is useful to sort the powers $\alpha_j^{(i)}$ for a given corner i in an ascending order of the real part $0 \leqslant \Re(\alpha_1^{(i)}) \leqslant \Re(\alpha_2^{(i)}) \leqslant \cdots$. For the rigid corners C and D, the exponent of the leading-order term is $\Re(\alpha_1^{(C,D)}) \approx 2.74$ [35]. However, the most dangerous contributions result from the two singular corners A and B for which $\alpha_j^{(A,B)} = j - 1$ [24]. If we now construct $\mathbf{u}_c$ as the sum of the two leading-order terms of both asymptotic solutions for the singular corners, the residuum $\mathbf{u}_*$ scales like $\sim r^{\alpha_3^{(A,B)}} = r^2$ as the corners A and B are approached. Hence, the convergence-rate exponent for the residuum becomes $\gamma = 2\alpha_3^{(A,B)} + 1 = 5$. The corresponding convergence rate $\sim \mathcal{O}(N^{-5})$ has been confirmed numerically by Bottela [7] and Bottela and Peyret [9].

In three dimensions, the construction of the function $\mathbf{u}_c$ is not so obvious. However, in the case of periodic boundary conditions a superposition of the two asymptotic edge solutions for $A = (-\Gamma/2, -1/2, z)$ and $B = (-\Gamma/2, 1/2, z)$ is possible, as for the two-dimensional flow, and the singularity in the boundary condition for the residuum $\mathbf{u}_*$ is reduced. Here, we shall employ the second-order approximation to the edge problem by Hancock et al. [27] and Gupta et al. [24] which also includes the leading-order inertia term. According to Botella and Peyret [9] one expects a reduction of the error like $\mathcal{O}(N^{-5})$, as in the two-dimensional case. For the practical implementation, the three-dimensional solution of the cavity-flow problem (1a, b) is written as [8]

$$\mathbf{u} = \mathbf{u}_*(x,y,z) + \mathbf{u}_c(x,y) = \mathbf{u}_* + \sum_{m\in\{A,B\}, n\in\{1,2\}} \mathbf{u}_c^{m,(n)}, \tag{14a}$$

$$p = p_*(x,y,z) + p_c(x,y) = p_* + \sum_{m\in\{A,B\}, n\in\{1,2\}} p_c^{m,(n)}, \tag{14b}$$

where the asymptotic solutions $(\mathbf{u}_c^{m,(n)}, p_c^{m,(n)})$ of order n for the edges $m \in \{A, B\}$ satisfy the equations

$$\nabla \cdot \mathbf{u}_c^{m,(1)} = 0, \tag{15a}$$

$$-\nabla p_c^{m,(1)} + \Delta \mathbf{u}_c^{m,(1)} = 0, \tag{15b}$$

$$\nabla \cdot \mathbf{u}_c^{m,(2)} = 0, \tag{15c}$$

$$-\nabla p_c^{m,(2)} + \Delta \mathbf{u}_c^{m,(2)} = \mathbf{u}_c^{m,(1)} \cdot \nabla \mathbf{u}_c^{m,(1)}, \tag{15d}$$

subject to the conditions $\mathbf{u}_c^{m,(1)} = Re\, \mathbf{e}_y$ on $x = -\Gamma/2$ and $\mathbf{u}_c^{m,(1)} = 0$ on the respective other boundary. $\mathbf{u}_c^{m,(2)}$ must satisfy homogeneous boundary conditions. By inserting this ansatz into the Navier–Stokes equations (1a) and (1b) we obtain

$$\frac{\partial}{\partial t}\mathbf{u}_* + \mathbf{u}_* \cdot \nabla \mathbf{u}_c + \mathbf{u}_c \cdot \nabla \mathbf{u}_* + \mathbf{u}_* \cdot \nabla \mathbf{u}_* + \mathcal{N}(\mathbf{u}_c, \mathbf{u}_c) = -\nabla p_* + \nabla^2 \mathbf{u}_*, \tag{16a}$$

$$\nabla \cdot \mathbf{u}_* = 0, \tag{16b}$$

with

$$\mathcal{N}(\mathbf{u}_c, \mathbf{u}_c) = \mathbf{u}_c^{(1)} \cdot \nabla \mathbf{u}_c^{(2)} + \mathbf{u}_c^{(2)} \cdot \nabla\left(\mathbf{u}_c^{(1)} + \mathbf{u}_c^{(2)}\right) + \mathbf{u}_c^{B,(1)} \cdot \nabla \mathbf{u}_c^{A,(1)} + \mathbf{u}_c^{A,(1)} \cdot \nabla \mathbf{u}_c^{B,(1)}, \tag{17a}$$

$$\mathbf{u}_c^{(1)} = \sum_{m\epsilon\{A,B\}} \mathbf{u}_c^{m,(1)}, \tag{17b}$$

$$\mathbf{u}_c^{(2)} = \sum_{m\epsilon\{A,B\}} \mathbf{u}_c^{m,(2)}. \tag{17c}$$

The boundary conditions in x- and y-directions for the residuum $\mathbf{u}_*$ are

$$\mathbf{u}_* = Re\,\mathbf{e}_y - \mathbf{u}_c \quad \text{on } x = -\Gamma/2, \tag{18a}$$

$$\mathbf{u}_* = -\mathbf{u}_c \quad \text{on } y = \pm 1/2. \tag{18b}$$

For periodic boundary conditions (7) remains unaltered. By subtracting the asymptotic edge solutions additional nonlinear terms are introduced in the time-integration scheme (12a)–(13c). It is now used to solve for $\mathbf{u}_*$ and p_*. It will be shown below that the convergence and the accuracy is significantly improved, as compared to a direct solution of $(\mathbf{u}, p)$.

Let us now consider the three-dimensional case with rigid end-wall condition. At first sight, it is tempting to superpose four solutions of Gomilko et al. [21] for the four corners and four edges to construct $\mathbf{u}_c$. A superposition with weighting factor 1, however, introduces new singularities which are not present in the original cavity-flow problem. Consider, for example, a superposition of the two local asymptotic solutions for the two upstream corners $(x, y, z) = (-\Gamma/2, -1/2, \pm\Lambda/2)$ of the moving lid. Then the singular edges $(x, z) = (-\Gamma/2, \pm\Lambda/2)$ along both end-walls are properly captured, but along the common edge $(x, y) = (-\Gamma/2, -1/2)$ of both upstream corners the singularity is taken care of twice! When the remaining two local asymptotic corner-flow solutions of both downstream corners $(x, y, z) = (-\Gamma/2, 1/2, \pm\Lambda/2)$ are added, also both edges $(x, z) = (-\Gamma/2, \pm\Lambda/2)$ along the moving plate with tangential singularities are taken care of twice. Hence, a superposition of the asymptotic corner solutions of the four singular corners $(x, y, z) = (-\Gamma/2, \pm 1/2, \pm\Lambda/2)$ with weighting factor 1/2 would remove all singularities on the edges of the cavity. However, the residual flow $\mathbf{u}^*$ on the rigid end-walls is singular as any corner is approached in the plane of each end-wall: For a given end-wall, there is no contribution to the residual $\mathbf{u}^*$ from the two asymptotic solutions of the two corners which have a plane in common with that end-wall. However, the contributions from the asymptotic solutions of the distant corners to the residual become singular as one of the corners of the end-wall under consideration is approached in the plane of that end-wall. From these considerations, we conclude that the singularities in the boundary conditions cannot be fully removed by subtracting one half of the asymptotic solutions for the four singular corners. We have not, however, investigated the effect of the remaining singularity on the convergence.

In view of these difficulties, we applied the two-dimensional asymptotic solutions of Hancock et al. [27] and Gupta et al. [24] also in the case of rigid end-walls. Compared to the previous case of periodic boundary conditions we have to modify the boundary conditions on the end-walls to

$$\mathbf{u}_* = -\mathbf{u}_c \quad \text{on } z = \pm\Lambda/2. \tag{19}$$

However, the two edges at $(x, z) = (-\Gamma/2, \pm\Lambda/2)$ between the moving wall and the end-walls remain singular. As will be shown later, the effect of these weaker singularities remains confined to regions near both end-walls and does not degrade the convergence in the bulk.

4. Code validation

As the first step, we validate the code by comparing our results for the usual *two-dimensional* flow ($w = \partial/\partial z = 0$) with those of Bottela and Peyret [8]. The calculations are performed for the square cavity with $\Gamma = 1$ and for $Re = 1000$. The initial conditions for the calculations on the coarsest grid were $\mathbf{u} = p = 0$. For all finer grids, the initial conditions were obtained by interpolating the converged result for a given grid onto the next finer grid.

For all span aspect ratios Λ, the flow for $t \to \infty$ was found to be steady. This is consistent with experimental evidence, as no two-dimensional oscillatory flow has ever been observed. As a criterion for the convergence to the steady time-asymptotic flow, we used the condition

$$\frac{\max_{x,y,z,i} |u_i(\mathbf{x}, t) - u_i(\mathbf{x}, t - \Delta t)|}{\Delta t |Re|} < \epsilon. \tag{20}$$

As soon as this condition was satisfied the time-integration was terminated and the flow field obtained was considered *steady*. For all calculations, we used $\epsilon = 10^{-7}$, if not specified otherwise.

All results of Bottela and Peyret [8], those including and those excluding the asymptotic corner solutions, could be reproduced to the given accuracy. As examples, the extremal velocities on the centerlines of the cavity are listed in Table 1 as functions of the resolution. The calculations were performed including the asymptotic corner solutions. Some remaining differences in the last significant digit result from the detection method of the location of the velocity extrema. Since we have used Newton's method, the extrema locations could be computed much more accurately ($\Delta x < 10^{-4}$) than by Bottela and Peyret [8].

To validate our *three-dimensional* code, we compared our results with those of Ku et al. [32]. They calculated the flow in a cubic cavity ($\Gamma = \Lambda = 1$) with rigid end-walls for $Re = 100$, 400, and 1000. Fig. 2 shows the velocity profiles along the centerlines $(x, 0, 0)$ and $(0, y, 0)$. The calculations were made by subtracting the two asymptotic edge solutions. Our data are in good agreement with the results of Ku et al. [32], even when using a low resolution. It will be shown in the next section that the extremal velocities on the centerlines obtained for the low resolution used for Fig. 2 differ less than 1% from the fully converged solution on a very fine grid.

The second comparison of three-dimensional flows is made for a cavity with $\Gamma = 2$ and $\Lambda = 1$ which was considered by Cortes and Miller [13]. In Fig. 3, the velocity profile $v(x, 0, 0)$ on the x-axis is shown for several Reynolds numbers. For $Re \leqslant 400$, our results (solid and dotted lines) are in very good agreement with those of Cortes and Miller [13] (indicated by symbols). However, for $Re = 1000$ both the magnitude and the location of the velocity minimum differ. This difference is substantial, since the velocity profile does not change visibly on the scale of Fig. 3 when increasing the resolution (see Fig. 7).

Table 1
Minimum and maximum velocities on the centerlines of the two-dimensional square cavity ($\Gamma = 1$) for different resolutions $N = N_x = N_y$

N	$\min_x v(x,0)$	x	$\max_y u(0,y)$	y	$\min_y u(0,y)$	y
48	−388.5271	0.3283	527.0170	0.4092	−376.8991	−0.3422
48†	−388.5271	0.3283	527.0168	0.4092	−376.8991	−0.3422
64	−388.5695	0.3283	527.0764	0.4092	−376.9440	−0.3422
64†	−388.5695	0.3283	527.0763	0.4092	−376.9439	−0.3422
96	−388.5698	0.3283	527.0773	0.4092	−376.9447	−0.3422
96†	−388.5698	0.3283	527.0771	0.4092	−376.9447	−0.3422
128	−388.5698	0.3283	527.0773	0.4092	−376.9447	−0.3422
128†	−388.5698	0.3283	527.0771	0.4092	−376.9447	−0.3422

The Reynolds number is $Re = 1000$. The values of Bottela [7] are marked with a dagger †.

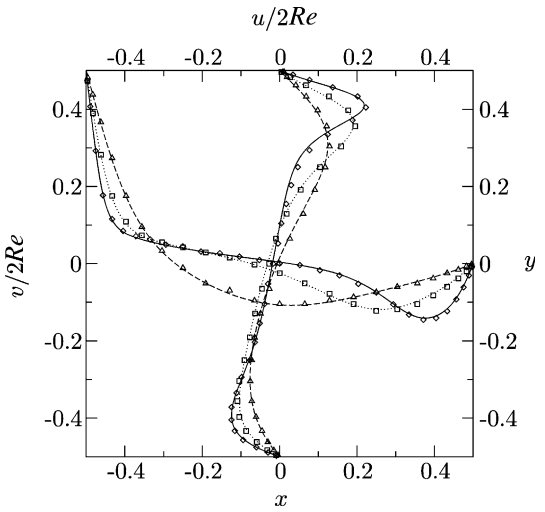

Fig. 2. Normal velocities on the centerlines $(x, 0, 0)$ and $(0, y, 0)$ in the cubic cavity for $\Gamma = \Lambda = 1$ using a resolution $N_x \times N_y \times N_z = 32 \times 32 \times 24$. The Reynolds numbers are $Re = 100$ (dashed line), $Re = 400$ (dotted line), and $Re = 1000$ (solid line). The symbols $\triangle$ ($Re = 100$), $\square$ ($Re = 400$), and $\diamond$ ($Re = 1000$) represent the results of Ku et al. [32], extracted from their figures.

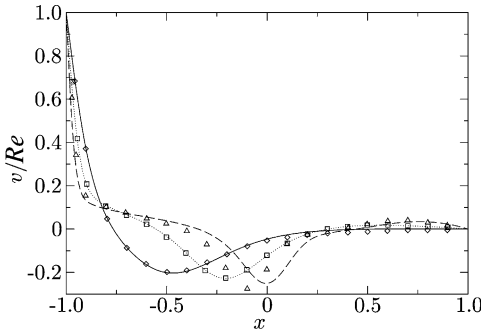

Fig. 3. Velocity profiles $v(x, 0, 0)$ for $\Gamma = 2$. The Reynolds numbers are $Re = 100$ (solid line, $\diamond$), $Re = 400$ (dotted line, $\square$) and $Re = 1000$ (dashed line, Δ). Symbols indicate the results of Cortes and Miller [13]. The resolution of the present calculation is $N_x \times N_y \times N_z = 32 \times 24 \times 16$.

The third comparison is made with results of Guermond et al. [23]. They have investigated the start-up flow in a rectangular cavity ($\Gamma = 1$) with a span aspect ratio $\Lambda = 2$ for $Re = 1000$ when the speed of the lid is increased suddenly from zero to its final value. We compare the time evolution of the velocity components $u(t)$ and $v(t)$ monitored at the six points $(0, y_{1,2}, z_i)$ and $(x_1, 0, z_i)$ for $i = 1, 2$. The coordinates $y_{1,2}$ and x_1 are selected to be close to the locations where u and v on the centerlines $(0, y, 0)$ and $(x, 0, 0)$ take their extrema. In Fig. 4(a) and (b), these velocities are plotted as functions of time in the planes $z_1 = 0$ (a) and $z_2 = 0.75$ (b). The present results, shown as lines, agree very well with the calculations of Guermond et al. [23] (symbols).

As a last validation, we make a comparison with the results of Albensoeder et al. [2]. By a linear stability analysis, they have calculated the critical parameters for the first instability of the two-dimensional flow in the lid-driven cavity with infinite span ($\Lambda \to \infty$) as a function of the aspect ratio Γ. They predicted the first instability in an infinitely long cavity to consist of three-dimensional Taylor–Görtler vortices. We carried

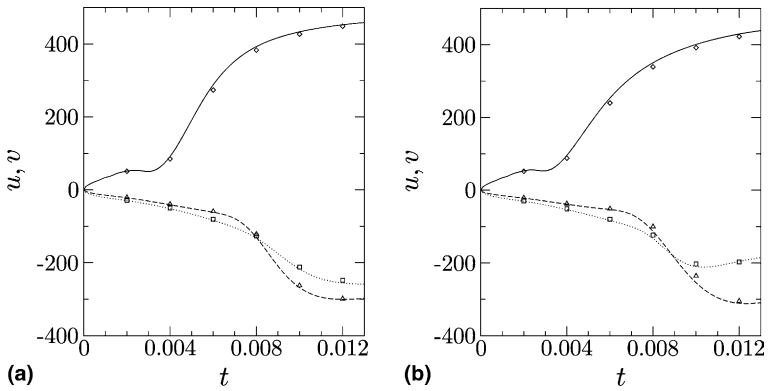

Fig. 4. Velocities $u(\mathbf{x}_1)$ (solid line, ◇), $u(\mathbf{x}_2)$ (dotted line, □), and $v(\mathbf{x}_3)$ (dashed line, Δ) as functions of time t for $Re = 1000$, $\Gamma = 1$, and $\Lambda = 2$. The velocities are monitored at $\mathbf{x}_1 = (0,0.40908, z)$, $\mathbf{x}_2 = (0, -0.27777, z)$, and $\mathbf{x}_3 = (0, -0.29797, z)$ with $z_1 = 0$ (a) and $z_2 = 0.75$ (b). The resolution is $N_x \times N_y \times N_z = 32 \times 32 \times 32$. Symbols indicate the results of Guermond et al. [23].

out simulations for $\Gamma = 1$ and periodic boundary conditions using different resolutions ($N_x \times N_y \times N_z = 30 \times 30 \times 19$ and $N_x \times N_y \times N_z = 42 \times 42 \times 25$). The aspect ratio Λ, i.e., the period in spanwise direction, was set to $\Lambda = 2\pi/k_c = 0.407$, where $k_c = 15.43$ is the critical wavenumber predicted by Albensoeder et al. [2]. To determine the onset of the three-dimensional flow, the Reynolds number was decreased quasi-statically using decrements of $\delta Re = 1$ until the Taylor–Görtler vortices vanished, leaving a pure two-dimensional flow. The three-dimensional flow was observed to diminish continuously with Re and vanished completely at $Re = 783 \pm 1$ for both resolutions. This value matches very well with the critical Reynolds number $Re_c = 786.3 \pm 6$ predicted by Albensoeder et al. [2].

In the next section, we shall prove the good convergence properties of the method. It will be demonstrated that the moderate resolutions used for the preceding validations are very close to the resolution for which the solution is fully converged, i.e., for which the error is less than $\delta\mathbf{u}/Re < 10^{-5}$.

5. Benchmark data for $Re = 1000$

It is well known that the geometry has a strong influence on the flow. For this reason, we shall provide benchmark data for $Re = 1000$ and the aspect ratios $(\Gamma, \Lambda) = (1, 1)$, $(1, 2)$, $(1, 3)$, and $(2, 1)$ which are commonly used in experiments and numerics. Most calculations have been performed for no-slip end-wall conditions. In addition, results for periodic boundary conditions will be provided for the cubic cavity $(\Gamma, \Lambda) = (1, 1)$. The flow was found to be steady in all cases considered.

5.1. No-slip end-walls

In the previous section, the velocities on the centerlines of a cubical cavity were presented for a moderate resolution. To illustrate the grid convergence the maximum velocity $\max_y u(0, y, 0)$ on the vertical centerline is plotted as a function of the resolution $N = N_x = N_y$ in Fig. 5 for a square cross-section $\Gamma = 1$ and several span aspect ratios Λ. Velocity values are provided for both approaches, direct calculations without making use of the asymptotic edge-flow solutions (connecting lines between symbols are dotted), and calculations including the asymptotic edge-flow solutions (lines are full, dashed or dash-dotted). The resolutions N_z in z-direction corresponding to N are provided in Tables 2–4. All velocity extrema were computed by Newton's method.

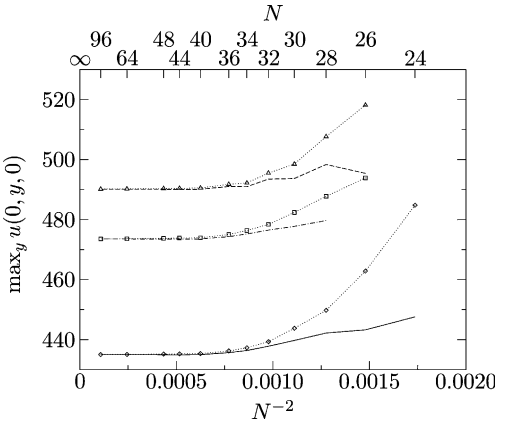

Fig. 5. Maximum $\max_y u(0, y, 0)$ as function of the resolution $N = N_x = N_y$ for $Re = 1000$, $\Gamma = 1$ and $A = 1$ (solid line), $A = 2$ (dash-dotted line), and $A = 3$ (dashed line) when the asymptotic edge-flow solution is utilized. Symbols ◇, □, and Δ indicate the convergence without employing the asymptotic solutions. The corresponding resolution in z-direction is listed in Tables 2–4.

Table 2
Minimum and maximum velocities on the centerlines $(x, 0, 0)$ and $(0, y, 0)$ for $\Gamma = A = 1$ and $Re = 1000$ in dependence of the number of grid points for calculations including the asymptotic solutions

$N_x \times N_y \times N_z$	$\max_y u$	y	$\min_y u$	y	$\min_x v$	x
$24 \times 24 \times 16$	447.5908	0.4107	−252.8331	−0.3895	−287.8303	0.3753
$26 \times 26 \times 18$	443.2833	0.4097	−251.1739	−0.3945	−287.1292	0.3757
$28 \times 28 \times 20$	442.2136	0.4102	−252.5244	−0.3928	−285.6441	0.3768
$30 \times 30 \times 22$	439.7417	0.4099	−249.4673	−0.3897	−283.9487	0.3763
$32 \times 32 \times 24$	437.8115	0.4097	−248.3688	−0.3919	−282.4369	0.3761
$34 \times 34 \times 26$	436.3667	0.4096	−247.6508	−0.3913	−281.4070	0.3759
$36 \times 36 \times 26$	435.6872	0.4096	−247.1098	−0.3908	−280.8462	0.3759
$48 \times 48 \times 32$	434.9667	0.4096	−246.6312	−0.3909	−280.3480	0.3758
$64 \times 64 \times 48$	435.0177	0.4096	−246.6517	−0.3909	−280.3830	0.3758
$96 \times 96 \times 64$	435.0186	0.4096	−246.6511	−0.3909	−280.3833	0.3758

Table 3
Minimum and maximum velocities on the centerlines $(x, 0, 0)$ and $(0, y, 0)$ for $Re = 1000$, $\Gamma = 1$, and $A = 2$ in dependence of the number of grid points for calculations including the asymptotic solutions

$N_x \times N_y \times N_z$	$\max_y u$	y	$\min_y u$	y	$\min_x v$	x
$28 \times 28 \times 28$	479.6984	0.4116	−299.7853	−0.3597	−324.7577	0.3683
$30 \times 30 \times 30$	477.7744	0.4108	−296.9597	−0.3636	−323.7770	0.3707
$32 \times 32 \times 32$	476.5096	0.4106	−295.3656	−0.3617	−322.3326	0.3706
$34 \times 34 \times 34$	475.2217	0.4107	−294.7815	−0.3601	−321.0739	0.3700
$36 \times 36 \times 36$	474.3428	0.4108	−294.5013	−0.3595	−320.3122	0.3696
$48 \times 48 \times 48$	473.5296	0.4108	−294.0667	−0.3588	−319.7264	0.3694
$64 \times 64 \times 64$	473.5843	0.4108	−294.0967	−0.3588	−319.7648	0.3694
$96 \times 96 \times 96$	473.5850	0.4108	−294.0967	−0.3588	−319.7651	0.3694

From Fig. 5, we can conclude that the inclusion into the ansatz of the asymptotic analytical solutions for the two-dimensional edge flows leads to an improved convergence (full, dashed, and dash-dotted lines), although the two edges $(-1/2, y, \pm A/2)$ between the moving plate and the rigid walls at $z = \pm A/2$ remain

Table 4
Minimum and maximum velocities on the centerlines $(x, 0, 0)$ and $(0, y, 0)$ for $Re = 1000$, $\Gamma = 1$, and $\Lambda = 3$ in dependence of the number of grid points for calculations including the asymptotic solutions

$N_x \times N_y \times N_z$	$\max_y u$	y	$\min_y u$	y	$\min_x v$	x
$26 \times 26 \times 26$	495.4298	0.4103	−328.3674	−0.3677	−351.0431	0.3580
$28 \times 28 \times 28$	498.3751	0.4097	−329.8616	−0.3828	−350.4184	0.3655
$30 \times 30 \times 30$	493.7083	0.4100	−327.1414	−0.3749	−347.7627	0.3629
$32 \times 32 \times 32$	493.4983	0.4096	−325.4250	−0.3778	−346.7478	0.3641
$34 \times 34 \times 34$	490.9682	0.4097	−324.6165	−0.3759	−345.4581	0.3628
$36 \times 36 \times 36$	491.0394	0.4097	−324.1757	−0.3768	−345.0945	0.3634
$48 \times 48 \times 48$	490.1092	0.4097	−323.5094	−0.3763	−344.4298	0.3633
$64 \times 64 \times 64$	490.1732	0.4097	−323.5474	−0.3763	−344.4592	0.3633
$96 \times 96 \times 96$	490.1725	0.4097	−323.5474	−0.3763	−344.4587	0.3633

singular. The acceleration of the convergence applies to all span aspect ratios considered ($\Lambda = 1, 2, 3$). It can be inferred from Tables 2–4 that the extrema of the other velocity components experience a similar improvement of the convergence rate. We did not explicitly tabulate the results obtained without subtracting the asymptotic solutions. A comparison of the numerical data from Tables 2–4 for the highest resolutions with those of half the resolution shows that the accuracy of the extremal velocities on the centerlines for the highest resolution is much better than $\delta\mathbf{u}/Re < 10^{-5}$. For future reference we also provide in Tables 5 and 6 the velocity values on the horizontal and vertical centerlines.

To check the global convergence, we employ the L^2_ω-norm of the velocity error

$$L^2_\omega(\mathbf{u}) = \frac{1}{Re}\left(\|u - u_{\mathrm{ref}}\|^2_{L^2_\omega} + \|v - v_{\mathrm{ref}}\|^2_{L^2_\omega} + \|w - w_{\mathrm{ref}}\|^2_{L^2_\omega}\right)^{1/2}, \tag{21}$$

where $\|u - u_{\mathrm{ref}}\|_{L^2_\omega}$, e.g., is defined by

$$\|u - u_{\mathrm{ref}}\|_{L^2_\omega} = \left(\int_\Omega |u(\mathbf{x}) - u_{\mathrm{ref}}(\mathbf{x})|^2 \xi(\mathbf{x})\, \mathrm{d}\mathbf{x}\right)^{1/2} \tag{22}$$

with $\Omega = [-\Gamma/2, \Gamma/2] \times [-0.5, 0.5] \times [-\Lambda/2, \Lambda/2]$ and the Chebyshev weight

$$\xi(\mathbf{x}) = \left\{\left[1 - \left(\frac{2}{\Gamma}x\right)^2\right]\left[1 - (2y)^2\right]\left[1 - \left(\frac{2}{\Lambda}z\right)^2\right]\right\}^{-1/2}. \tag{23}$$

The integrals like (22) were approximated by the Gauss–Lobatto formula for which the flow was interpolated on a Gauss–Lobatto grid of size $M \times M \times M$. In this case, we choose $M = 250$. The reference velocity $\mathbf{u}_{\mathrm{ref}}$ is taken as the result obtained using the highest resolution ($\Lambda = 1$: $N_x \times N_y \times N_z = 96 \times 96 \times 64$, $\Lambda = 2, 3$: $N_x \times N_y \times N_z = 96 \times 96 \times 96$). In Fig. 6(a), the L^2_ω-norm is plotted as a function of the grid size $N = N_x = N_y$ (for N_z see Tables 2–4) for the span aspect ratios $\Lambda = 1$, $\Lambda = 2$, and $\Lambda = 3$. It can be seen that the global convergence is not as good as the point-wise convergence, as discussed before. We find that the L^2_ω-error scales like $N^{-1.4}$ and $N^{-1.5}$ for calculations including, the asymptotic solutions into and excluding them from the ansatz, respectively. The obtained convergence rates are significantly lower than the rate $N^{-5.1}$ at which the two-dimensional calculations of Bottela [7] converge when the edge singularities are taken into account.

To better understand the convergence rate of the L^2_ω-norm, we assume that the analysis of Botella and Peyret [9] for the two-dimensional flow, briefly summarized in Section 3.2, can also be applied to the three-dimensional case with rigid end-walls. Using spherical polar coordinates (r, θ, ϕ) centered at one of the singular corners $i \in \{A, B, C, D\}$ between the moving and two stationary walls and located at $(x, y, z) = (-\Gamma/2, \pm 1/2, \pm\Lambda/2)$, the leading-order term of the asymptotic series solution of the corner flow can be written as $\mathbf{u}_1^{(i)} = r^{\alpha_1^{(i)}} \mathbf{f}_1^{(i)}(\theta, \phi)$. According to Gomilko et al. [21], the exponent of this leading-order term is $\alpha_1^{(i)} = 0$.

Table 5
Velocity v and pressure p on the x-axis (x, 0, 0) for $Re = 1000$ and $\Gamma = 1$

x	Rigid boundary conditions						Periodic boundary conditions			
	$\Lambda = 1$ ($96 \times 96 \times 64$)		$\Lambda = 2$ ($96 \times 96 \times 96$)		$\Lambda = 3$ ($96 \times 96 \times 96$)		$\Lambda = 1$ ($96 \times 96 \times 65$)			
	v/Re	p/Re^2	v/Re	p/Re^2	v/Re	p/Re^2	v/Re	p/Re^2	v/Re	p/Re^2
−0.5000	1.0000000	0.008645	1.0000000	0.020067	1.0000000	0.020722	1.0000000	0.044676	1.0000000	0.041666
−0.4766	0.5896414	0.007985	0.6081626	0.019151	0.6366360	0.019972	0.5992648	0.043278	0.6692592	0.041548
−0.4688	0.4844275	0.007755	0.5111673	0.018791	0.5453499	0.019636	0.5029417	0.042746	0.5822494	0.041329
−0.4609	0.3982086	0.007531	0.4352362	0.018419	0.4730371	0.019273	0.4310361	0.042190	0.5098953	0.041030
−0.4531	0.3317110	0.007322	0.3800975	0.018048	0.4197163	0.018899	0.3823946	0.041627	0.4532512	0.040668
−0.3516	0.1218293	0.005161	0.2124395	0.011821	0.2368726	0.011810	0.2850062	0.030148	0.2969424	0.029833
−0.2344	0.0733444	0.002575	0.1037698	0.004462	0.1103051	0.003305	0.1753694	0.010931	0.1711830	0.011051
−0.1172	0.0390483	0.000676	0.0333083	0.000796	0.0270859	−0.000415	0.0550436	−0.000189	0.0588776	0.000002
0.0000	0.0080177	0.000000	−0.0129662	0.000000	−0.0325844	0.000000	−0.0474572	0.000000	−0.0474130	−0.000105
0.0469	−0.0061192	0.000125	−0.0305044	0.000402	−0.0557138	0.001222	−0.0861502	0.003326	−0.0896886	0.003090
0.2187	−0.1099894	0.004171	−0.1385097	0.007472	−0.1775706	0.013128	−0.2277646	0.030482	−0.2607131	0.030750
0.3281	−0.2516006	0.016181	−0.2937825	0.025856	−0.3247462	0.035607	−0.3435525	0.060394	−0.3243194	0.064798
0.3984	−0.2729293	0.027919	−0.3054909	0.042697	−0.3223165	0.054662	−0.3518084	0.078688	−0.1937646	0.078983
0.4297	−0.2369550	0.031509	−0.2586761	0.047504	−0.2681329	0.059966	−0.3133212	0.084802	−0.1444237	0.082238
0.4375	−0.2228255	0.032121	−0.2418095	0.048304	−0.2500846	0.060842	−0.2976668	0.086044	−0.1326928	0.082837
0.4453	−0.2062332	0.032616	−0.2225479	0.048948	−0.2299980	0.061548	−0.2786265	0.087135	−0.1205861	0.083329
0.5000	0.0000000	0.033402	0.0000000	0.050114	0.0000000	0.062909	0.0000000	0.090742	0.0000000	0.083463

The results for periodic boundary conditions are listed for the two different planes z_0: = 0 (left two columns) and $z_1 = z_0 + \Lambda/6 = 1/6$ where $w = 0$ (two rightmost columns).

Table 6
Velocity u and pressure p on the y-axis (0, y, 0) for $Re = 1000$ and $\Gamma = 1$

y	Rigid boundary conditions						Periodic boundary conditions			
	$\Lambda = 1$ $(96 \times 96 \times 64)$		$\Lambda = 2$ $(96 \times 96 \times 96)$		$\Lambda = 3$ $(96 \times 96 \times 96)$		$\Lambda = 1$ $(96 \times 96 \times 65)$			
	u/Re	p/Re^2	u/Re	p/Re^2	u/Re	p/Re^2	u/Re	p/Re^2	u/Re	p/Re^2
0.5000	0.0000000	0.016579	0.0000000	0.029586	0.0000000	0.038752	0.0000000	0.059901	0.0000000	0.059339
0.4688	0.1886420	0.017524	0.2103534	0.030661	0.2123895	0.039937	0.2093464	0.061189	0.2116072	0.060555
0.4609	0.2409470	0.017543	0.2685775	0.030622	0.2727182	0.039886	0.2697260	0.061164	0.2709983	0.060409
0.4531	0.2903172	0.017395	0.3229981	0.030348	0.3294425	0.039566	0.3273820	0.060861	0.3256542	0.059923
0.4453	0.3351117	0.017045	0.3716805	0.029799	0.3804404	0.038926	0.3805818	0.060220	0.3730932	0.059039
0.4063	0.4342302	0.012298	0.4720530	0.023183	0.4893166	0.031157	0.5241776	0.051727	0.4493780	0.049489
0.3594	0.3111715	0.005326	0.3472198	0.013879	0.3752690	0.019871	0.4488558	0.037214	0.3433904	0.036685
0.3047	0.1522299	0.001560	0.2042160	0.008105	0.2420601	0.012018	0.3097281	0.025039	0.2620630	0.026029
0.0000	−0.0367355	0.000000	0.0006955	0.000000	−0.0096889	0.000000	−0.0309846	0.000000	−0.0287666	−0.000105
−0.2656	−0.1698661	0.008512	−0.2378601	0.013386	−0.2263912	0.015064	−0.2889870	0.037437	−0.3199535	0.037979
−0.2734	−0.1758025	0.008976	−0.2461943	0.014487	−0.2363559	0.016183	−0.2927245	0.039189	−0.3252668	0.040065
−0.3437	−0.2292360	0.014044	−0.2924917	0.025245	−0.3120431	0.028294	−0.3058621	0.052408	−0.2798443	0.053461
−0.4062	−0.2440743	0.018959	−0.2773856	0.033133	−0.3125534	0.038760	−0.3028215	0.060587	−0.2337254	0.059340
−0.4219	−0.2350273	0.019929	−0.2627359	0.034518	−0.2969139	0.040643	−0.3018496	0.062729	−0.2186192	0.061021
−0.4297	−0.2274623	0.020337	−0.2528278	0.035096	−0.2859568	0.041419	−0.3003886	0.063779	−0.2091965	0.061792
−0.4375	−0.2173841	0.020691	−0.2405949	0.035596	−0.2723632	0.042083	−0.2970567	0.064784	−0.1980795	0.062467
−0.5000	0.0000000	0.021761	0.0000000	0.037086	0.0000000	0.043698	0.0000000	0.068843	0.0000000	0.062829

The results for periodic boundary conditions are listed for the two different planes z_0: = 0 (two left columns) and $z_1 = z_0 + \Lambda/6 = 1/6$ where $w = 0$ (two rightmost columns).

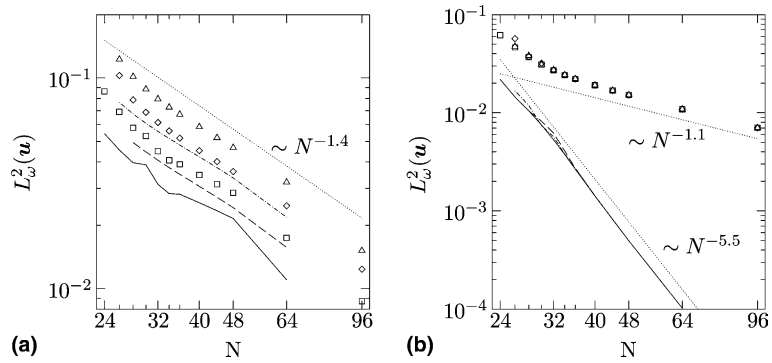

Fig. 6. (a) L^2_ω-norm of the error as function of the grid size for $N = N_x = N_y$ for different runs including (lines) and excluding (symbols) the asymptotic solution in the ansatz. Symbols and lines denote the following span aspect ratios. Full line, □: $\Lambda = 1$; dashed line, ◇: $\Lambda = 2$; and dash-dotted line, Δ: $\Lambda = 3$. The interpolation grid size for the integration is $M = 250$. (b) Same as (a), but restricted to the (x, y)-plane $z = 0$ with $\Omega_{z=0} = [-\Gamma/2, \Gamma/2] \times [-0.5, 0.5]$. The dotted lines indicate the asymptotic power laws.

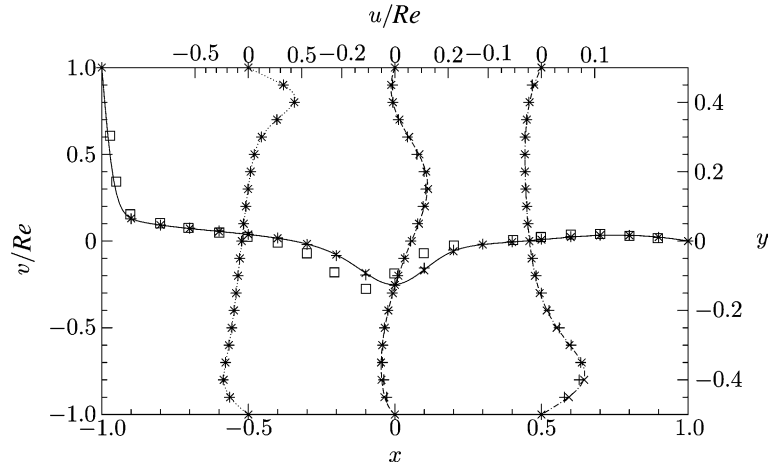

Fig. 7. Velocity profiles $v(x, 0, 0)$ (solid line), $u(-0.5, y, 0)$ (dotted line), $u(0, y, 0)$ (dashed line), and $u(0.5, y, 0)$ (dash-dotted line) normalized by $Re = 1000$ for $\Gamma = 2$ and $\Lambda = 1$ with $N_x \times N_y \times N_z = 96 \times 96 \times 96$. The symbols □ indicate the results of Cortes and Miller [13] extracted from their figures. To indicate convergence the symbols + and × denotes the results for $N_x \times N_y \times N_z = 32 \times 24 \times 16$ and $N_x \times N_y \times N_z = 48 \times 32 \times 32$, respectively.

Keeping in mind that the singularities along the edges between the moving wall and the end-walls are not removed by our present approach one would expected $\gamma \approx 2\alpha_1^{(i)} + 1 = 1$ to be a first approximation to the numerical error. Our calculations yield $\gamma = 1.4$ and $\gamma = 1.5$ for the both cases. This result seems to confirm the approach of Botella and Peyret [9], even though the exponent γ of the convergence rate obtained here for the three-dimensional case is about 50% larger than expected. This conclusion is also supported by the fact that the convergence rate is practically independent of whether the asymptotic solutions are subtracted or not.

The convergence of the numerical solution is much better, however, in the interior of the 3D cavity than close to the end-walls at $z = \pm\Lambda/2$, each containing a weakly singular edge. This can be seen from Fig. 6(b) in which the L^2_ω-norm of the error restricted to the (x, y)-plane $z = 0$ (i.e., $\Omega_{z=0} = [-\Gamma/2, \Gamma/2] \times [-0.5, 0.5]$) is plotted as a function of $N = N_x = N_y$. It decreases approximately like $N^{-5.5}$. This must be compared with

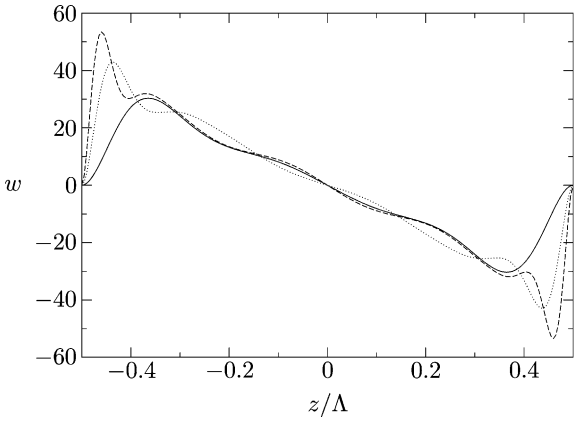

Fig. 8. Velocity profiles $w(0, 0, z)$ for $\Lambda = 1$ (solid line), $\Lambda = 2$ (dotted line), and $\Lambda = 3$ with $Re = 1000$ and $\Gamma = 2$. The resolution is $96 \times 96 \times 64$ for $\Lambda = 1$ and $96 \times 96 \times 96$ for $\Lambda = 2,3$.

the weak convergence $\sim N^{-1.1}$ of the L^2_ω-norm restricted to the (x, y)-plane when the asymptotic solutions are not taken into account (symbols is Fig. 6(b)).

Fig. 8 shows the accurate axial velocity $w(0, 0, z)$ of the vortex flow in the cavity for three different span aspect ratios Λ. Owing to the no-slip conditions on $z = \pm\Lambda/2$ secondary flows are induced. The corresponding Bödewadt layers at $z = \pm\Lambda/2$ are clearly exhibited, even for $\Lambda = 1$. While the axial velocity of the self-similar solution of Bödewadt [6] approaches a finite value far away from the rigid end-wall, the axial velocity exhibits, apart from slight oscillations, a linear profile in central region of the cavity. The slope of the profile is correlated with the strength of the Bödewadt pumping at the rigid walls, hence the curves for different aspect ratios approximately fall onto each other when scaling of the cavity depth by Λ, as in Fig. 8. Also visible is a weak and damped spatial oscillation of the axial velocity. This feature is in common with Bödewadt's similarity solution, albeit the spatial frequency is modified to some degree owing to the finite aspect ratio $\Lambda < \infty$.

The most obvious advantage of the inclusion of the asymptotic edge-flow solution into the ansatz is the significantly reduced error for low resolutions, as compared to calculations without the use of the asymptotic solutions. This behavior justifies the use of the relatively low resolutions for the validations in Section 4. If, however, the resolution is too low, the use of the asymptotic edge-flow solutions may lead to numerical instability of the time-integration, while the conventional method remains stable. Such a behavior was observed, e.g., for $\Lambda = 2$ and $N = 26$.

Finally, we consider no-slip end-wall boundary conditions for a cavity with $\Gamma = 2$ and $\Lambda = 1$. As mentioned in Section 4, our results deviate from those of Cortes and Miller [13] (see Fig. 3). An update of the velocity profile on the horizontal centerline using a resolution of $N = N_x = N_y = N_z = 96$ is given in Fig. 7. In addition, the vertical velocity profiles $v(\pm 0.5, y, 0)$ and $v(0, y, 0)$ are included into the graph. To illustrate convergence the numerical results for two different lower resolutions, indicated by the symbols + and ×, are overlayed in the plot. Selected numerical velocity values of these profiles are given in Table 7.

5.2. Periodic boundary conditions

As an example for periodic boundary conditions at $z = \pm\Lambda/2$, we consider the flow in a cubic unit cell, i.e., $\Gamma = \Lambda = 1$. Albensoeder et al. [2] have shown that the steady two-dimensional flow in a cavity with a square cross-section becomes unstable to steady short-wavelength Taylor–Görtler vortices when the system is unbounded in z-direction ($\Lambda \to \infty$). The critical parameters are $Re_c = 786.3 \pm 6$ and $k_c = 15.43 \pm 0.06$. By

Table 7
Velocity components v and u and the pressure p on the x- and y-axes $(x, 0, 0)$ and $(0, y, 0)$, respectively

x	$y = 0$		y	$x = -0.5$		$x = 0$		$x = 0.5$	
	v/Re	p/Re^2		u/Re	p/Re^2	u/Re	p/Re^2	u/Re	p/Re^2
−1.00	1.000000	−0.013616	−0.50	0.000000	−0.013082	0.000000	0.027151	0.000000	0.009825
−0.97	0.470716	−0.014570	−0.46	−0.143892	−0.012960	−0.033922	0.025846	0.041546	0.010005
−0.95	0.273838	−0.015147	−0.41	−0.226613	−0.013521	−0.047906	0.023217	0.076012	0.009916
−0.90	0.130246	−0.016258	−0.36	−0.218455	−0.014703	−0.051561	0.018880	0.078266	0.009415
−0.80	0.092321	−0.018363	−0.30	−0.182022	−0.016219	−0.047193	0.012986	0.053258	0.008712
−0.50	0.038041	−0.023045	−0.16	−0.118605	−0.019769	−0.011378	0.002622	−0.000386	0.008300
−0.25	−0.042939	−0.020951	−0.07	−0.086136	−0.021883	0.026312	−0.000081	−0.015658	0.008587
−0.10	−0.184269	−0.012106	0.00	−0.060967	−0.023045	0.062110	0.000000	−0.022291	0.008850
0.00	−0.250511	0.000000	0.10	−0.023179	−0.023847	0.110966	0.003167	−0.027906	0.009172
0.10	−0.165149	0.007777	0.20	0.022083	−0.023769	0.115483	0.007470	−0.030658	0.009418
0.20	−0.057754	0.008974	0.30	0.124992	−0.022675	0.051995	0.008953	−0.029947	0.009595
0.50	0.008249	0.008850	0.40	0.428282	−0.016489	−0.007772	0.008527	−0.022182	0.009699
0.75	0.034290	0.009837	0.45	0.324198	−0.012621	−0.014091	0.008363	−0.013421	0.009732
1.00	0.000000	0.010163	0.50	0.000000	−0.013291	0.000000	0.008358	0.000000	0.009768

The parameters are $Re = 1000$, $\Gamma = 2$ and $\Lambda = 1$. The resolution is $N_x \times N_y \times N_z = 96 \times 96 \times 96$.

restricting the periodicity to $\Lambda = 1$ the Taylor–Görtler vortices bifurcate out of the basic flow at $Re_c^{\Lambda=1} = 828.5 \pm 1$, and a flow state with three Taylor–Görtler vortex pairs with wavelength $\lambda_c^{\Lambda=1} = 1/3$ ($k_c^{\Lambda=1} = 6\pi = 18.85$) is critical. It turns out that these steady Taylor–Görtler vortices are robust and remain stable at $Re = 1000$, dominating the whole flow structure.

To analyze the flow field, we decompose the dependence on z of each velocity component into Fourier modes $a_m(x, y)e^{imkz}$. The real amplitudes are then given by $A_m(x, y) = |a_m(x, y)|$. To demonstrate the convergence, the maxima with respect to x and y of the amplitudes of the velocity components of the Fourier mode $m = 3$ are plotted as functions of the resolution $N = N_x = N_y$ in Fig. 9. The corresponding resolution N_z in z-direction is provided in Table 8. Similar as for no-slip boundary conditions the use of the asymptotic

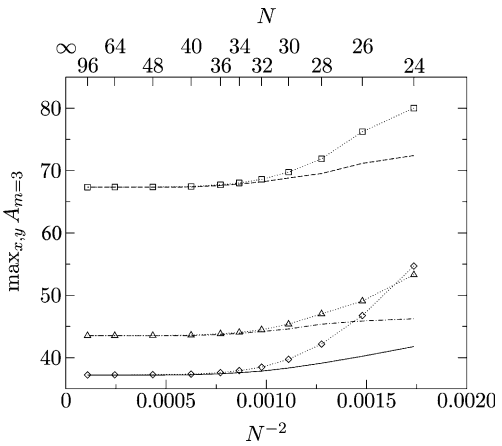

Fig. 9. Amplitude $\max_{x,y} A_{m=3}$ of the velocity components u (solid line), v (dashed line), and w (dash-dotted line) in the periodic cube ($\Gamma = 1$, $\Lambda = 1$) as functions of the resolution $N = N_x = N_y$ for $Re = 1000$, including the asymptotic edge-flow solution. Symbols ◇, □ and Δ, connected by dotted lines, indicate the corresponding values without the use of the asymptotic solutions. The respective resolutions in z direction are listed in Table 8.

Table 8
Maximum amplitudes of the constant mode ($m = 0$) of the velocities v and u on the positive x- and y-axis in dependence of the grid resolution

$N_x \times N_y \times N_z$	$\max_y A_{u,m=0}$	y	$\max_{x>0} A_{v,m=0}$	x	$\mathcal{O}(\epsilon)$
$24 \times 24 \times 17$	496.2805	0.4093	343.4480	0.3228	10^{-3}
$26 \times 26 \times 19$	493.3473	0.4081	344.2996	0.3248	$<10^{-7}$
$28 \times 28 \times 21$	492.9590	0.4086	344.1470	0.3246	10^{-5}
$30 \times 30 \times 23$	491.4466	0.4085	343.1649	0.3248	10^{-7}
$32 \times 32 \times 25$	490.3391	0.4084	342.3138	0.3250	10^{-3}
$34 \times 34 \times 27$	489.1522	0.4083	341.7372	0.3251	$<10^{-7}$
$36 \times 36 \times 27$	488.6639	0.4084	341.3982	0.3251	$<10^{-7}$
$48 \times 48 \times 33$	488.1099	0.4083	341.0659	0.3250	$<10^{-7}$
$64 \times 64 \times 49$	488.1580	0.4083	341.0920	0.3251	$<10^{-7}$
$96 \times 96 \times 65$	488.1588	0.4083	341.0921	0.3251	$<10^{-7}$

The parameters are $Re = 1000$, $\Gamma = 1$, and $\Lambda = 1$. The data are given for periodic boundary conditions including the asymptotic solutions.

solutions improves the convergence. The numerical effort can be reduced significantly if the accuracy requirements are relaxed to some degree, allowing the use of a lower resolution.

It is interesting to note that the Taylor–Görtler vortices calculated at low resolution are not exactly steady. The vortices as a whole are very slowly drifting in z-direction. Therefore, the termination criterion (20) with $\epsilon = 10^{-7}$ cannot be reached and the criterion had to be relaxed. The order of magnitude of ϵ required to terminate the time-integration is tabulated in Table 8 together with the amplitude data. From ϵ and the time-step Δt, the order of magnitude of the phase speed of the artificial drift can be obtained. For resolutions larger than $N_x = N_y = 32$ ($N_z = 25$) the calculated Taylor–Görtler vortices are found to be steady as $t \to \infty$ and we were able to apply the previously used termination criterion $\epsilon = 10^{-7}$. Note, however, that the minute drift practically does not change the good convergence of the method for low resolutions.

A quantitative convergence study is provided in Table 8. The maximum amplitudes of the constant Fourier mode $m = 0$, representing the two-dimensional part of the flow, are tabulated. Similar as for no-slip boundary conditions, the accuracy of the Fourier mode $m = 0$ at the highest resolution is better than $\delta A_{m=0}/Re < 10^{-5}$. A comparable accuracy and convergence rate is obtained for the Fourier mode $m = 3$. Values of the amplitude $A_{m=3}$ at the (x, y)-location at which the fundamental mode $m = 0$ reaches its maximum are given in Table 9.

Table 9
Amplitudes of the third harmonic ($m = 3$) of the velocity components u and v in dependence of the resolution

$N_x \times N_y \times N_z$	$A_{u,m=3}\vert_{\max_y A_{u,m=0}}$	$A_{v,m=3}\vert_{\max_{x>0} A_{v,m=0}}$
$24 \times 24 \times 17$	20.0578	3.6096
$26 \times 26 \times 19$	19.4779	3.5000
$28 \times 28 \times 21$	18.4349	3.0890
$30 \times 30 \times 23$	18.1826	3.0406
$32 \times 32 \times 25$	18.0651	3.0939
$34 \times 34 \times 27$	17.9293	3.1619
$36 \times 36 \times 27$	17.8617	3.1497
$48 \times 48 \times 33$	17.7922	3.1366
$64 \times 64 \times 49$	17.7952	3.1395
$96 \times 96 \times 65$	17.7953	3.1394

The values are taken on the positive y and x axis, respectively, where the constant mode ($m = 0$) takes its maximum (see table 8). The parameters and conditions are the same as for Table 8.

A global criterion for the convergence is the L^2_ω-norm of the amplitudes

$$L^2_\omega(\mathbf{A}) = \frac{1}{Re}\left(\|A_u - A_{u,\mathrm{ref}}\|^2_{L^2_\omega} + \|A_v - A_{v,\mathrm{ref}}\|^2_{L^2_\omega} + \|A_w - A_{w,\mathrm{ref}}\|^2_{L^2_\omega}\right)^{1/2}, \tag{24}$$

where, e.g., $\|A_u - A_{u,\mathrm{ref}}\|_{L^2_\omega}$ is defined by

$$\|A_u - A_{u,\mathrm{ref}}\|_{L^2_\omega} = \left(\sum_{m=0}^{(N_z-1)/2-1} \int_\Omega |A_{u,m}(\mathbf{x}) - A_{u,m,\mathrm{ref}}(\mathbf{x})|^2 \xi(\mathbf{x})\, \mathrm{d}\mathbf{x}\right)^{1/2} \tag{25}$$

with $\Omega = [-0.5, 0.5]^2$ and the weight ($\Gamma = 1$)

$$\xi(\mathbf{x}) = \left\{\left[1 - (2x)^2\right] \cdot \left[1 - (2y)^2\right]\right\}^{-1/2}. \tag{26}$$

As reference quantities the amplitudes obtained on the grid $N_x \times N_y \times N_z = 96 \times 96 \times 65$ are used, which have been computed by including the asymptotic edge-flow solutions into the ansatz. The integrals are approximated by sums using the Gauss–Lobatto formula for an interpolation grid with $M \times M$ nodes.

In Fig. 10, the L^2_ω-norm is plotted as a function of the grid size $N = N_x = N_y$ (for N_z see Table 8) for the cases in which the asymptotic solution is included in (solid line, □) and excluded from the ansatz (dashed line, ◇). To estimate the error caused by the finite sums entering the norm, the L^2_ω-norm has been calculated on two different interpolation grids, $M = 180$ (lines) and $M = 400$ (symbols). Both interpolations yield nearly identical results. Hence, the error associated with the calculation of the norm can be neglected for the present purpose.

From Fig. 10 the calculations including the asymptotic edge-flow solutions into the ansatz converge algebraically like $\sim N^{-5.7}$. The convergence rate without the inclusion of the asymptotic solutions is much weaker and approximately $\sim N^{-\gamma}$ with $\gamma = 1.1$. These convergence-rate exponents γ for periodic three-dimensional cavity flows are in good agreement with the results of Bottela [7] and Botella and Peyret [9] obtained for two-dimensional cavity flow (see the discussion in Section 5.1). Numerically they obtained $\gamma = 5.1$ when including, and $\gamma = 1.1$ when excluding the asymptotic solutions. Our results for three-dimensional flow also confirm the relation $\gamma = 2\alpha + 1$ of Bottela and Peyret [9] between the convergence-rate exponent γ and the exponent α of the strongest edge-flow singularity which is $\alpha = 2$ when the two leading-order terms of the asymptotic edge-flow solution are included into the ansatz as described in Section 3.2.

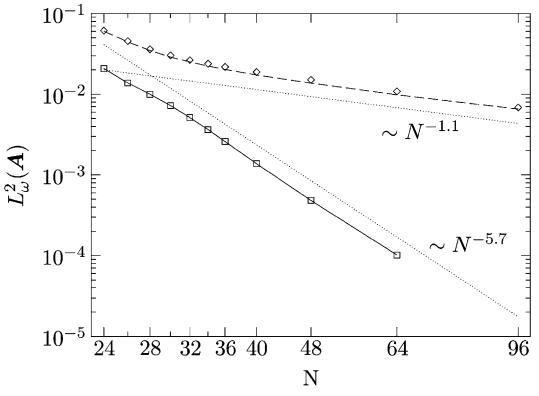

Fig. 10. L^2_ω-norm of the amplitudes as functions of the number of grid points $N = N_x = N_y$ with (full line, □) and without (dashed line, ◇) using the asymptotic solutions. The dotted lines indicate the respective power laws $N^{-5.7}$ and $N^{-1.1}$. The interpolation grid sizes used to calculate the norms are $M = 180$ (lines) and $M = 400$ (symbols).

Finally, the velocity components on the centerlines $(x, 0, z_i)$ and $(0, y, z_i)$ are listed in Tables 5 and 6 for two planes $i = 0,1$. When using periodic boundary condition in z-direction the phase of the three-dimensional flow is not fixed. To eliminate the phase the data are evaluated at two characteristic locations z_i relative to the periodic flow. In the present case the three-dimensional flow consists of steady rectangular cells in form of Taylor–Görtler-vortices. In agreement with Albensoeder et al. [2] we find that the velocity component w periodically vanishes on the cell boundaries, i.e. on planes $z = \text{const.}$, equidistantly spaced by $\Delta z = \lambda/2 = \Lambda/6$, where λ is the wavelength of the Taylor–Görtler vortices. Midway between two successive planes w as a function of z has an extremum. The reference planes $z_i = \text{const.}$ for which the velocity data are given in Tables 5 and 6 are successive planes on which $\partial_z w = 0$ $(i = 0)$ and $w = 0$ $(i = 1)$, i.e., $z_1 = z_0 + \Lambda/6$. Since three pairs of Taylor–Görtler vortices fit the full periodicity length Λ, there are six pairs of planes like z_0 and z_1. Although the periodicity is strictly enforced only every sixth plane we find the flow to be exactly periodic with period $\lambda = \Lambda/3$. For future comparison note, however, that the velocity components u and v take different values on two successive plane of the same type (either $\partial_z w = 0$ or $w = 0$), because the velocity field of the three-dimensional Taylor–Görtler vortices which is superposed on the two-dimensional part of the flow alternates with period λ. For the sake of brevity we have only presented one possibility in Tables 5 and 6 and omitted the data for the other case.

6. Conclusion

We have presented an efficient numerical method for calculating three-dimensional lid-driven cavity flows using pure Chebyshev collocation for rigid boundary conditions in the spanwise z-direction and a mixed Chebyshev-collocation–Fourier method for periodic boundary conditions in z-direction. Both methods represent extensions of the work of Botella and Peyret [8] to three-dimensions. In order to improve the accuracy of the spectral methods the singularities that the exact solution exhibits along the edges on which the boundary conditions are not continuous have been partly reduced. This was accomplished in a similar manner as in Botella and Peyret [8] by subtracting the leading-order singularities of the asymptotic edge-flow solutions for the edges along which the normal velocity is discontinuous. Numerical solutions were then calculated for the residual flow field which is less singular than the full flow field. We have provided highly accurate data for a number of representative three-dimensional cavity flows for Reynolds number $Re = 1000$ and various aspect ratios. A number of important flow data are summarized in Table 10.

Table 10
Extremal velocities on the centerlines of the cavity for selected span aspect ratios Λ

	Rigid b.c.			Periodic b.c.	
	$\Lambda = 1$ $(96 \times 96 \times 64)$	$\Lambda = 2$ $(96 \times 96 \times 96)$	$\Lambda = 3$ $(96 \times 96 \times 96)$	$\Lambda = 1$ $(96 \times 96 \times 65)$	
max u/Re	0.4350186	0.4735850	0.4901725	0.5260779	0.4550700
At $\mathbf{x} = (0, y, 0)$	0.40957	0.41077	0.40967	0.40097	0.41524
minu/Re	−0.2466511	−0.2940967	−0.3235474	−0.3058705	−0.3283077
At $\mathbf{x} = (0, y, 0)$	−0.39087	−0.35883	−0.37629	−0.34152	−0.28487
min v/Re	−0.2803833	−0.3197651	−0.3444587	−0.3617047	−0.3411548
At $\mathbf{x} = (x, 0, 0)$	0.37581	0.36944	0.36334	0.37024	0.30060
min w/Re	−0.0303398	−0.0429372	−0.0534788	−0.0007703	−0.0007703
At $\mathbf{x} = (0, 0, z)$	0.36492	0.87423	1.37922	0.25149	0.25149

The x and y locations of the extrema of u and v for periodic boundary conditions are taken in the plane $z_0 = 0$ (left column) and in the plane $z_1 = z_0 + \Lambda/6 = 0.1\bar{6}$ (right column) in which the velocity component w vanishes. All calculations were made including the asymptotic solutions.

For periodic end-wall boundary conditions the residual flow satisfies much smoother boundary conditions than the full flow field. Hence, the numerical solution for the residual flow converges much faster than the conventional solution which does not take into account the specific flow structure near the singular edges. Even at moderate resolutions a significant gain in accuracy is obtained. In particular, we provided benchmark data for periodic three-dimensional Taylor–Görtler vortices in the unit cube at Reynolds number $Re = 1000$. This case is typical for three-dimensional flow structures generated by bulk flow instabilities.

For rigid end-wall boundary conditions not all edge and and corner singularities can be removed by a simple subtraction. Therefore, significant singularities of the tangential velocity remain along the edges formed by the moving lid and the end-walls. Global convergence studies show that the remaining tangential-flow singularities at the end walls annihilate the positive effect obtained by subtracting the leading-order singularities associated with the normal-velocity discontinuities. This effect is particularly important in the vicinity of the end-walls. In the bulk of the cavity, however, the effect of the end-wall singularities is less pronounced and a substantial convergence acceleration is obtained locally. Regardless of the end-wall boundary conditions, our convergence studies confirm the result of Bottela and Peyret [9] who related the exponent γ of the error $\mathcal{O}(N^{-\gamma})$ of Chebyshev methods to the smallest real part of the exponent α of the asymptotic edge solution of the form $u = r^{\alpha} f(\theta)$.

Of course, an elimination of the leading-order singular terms by subtracting them from the full solution is highly desirable for the rigid-boundary case. Because this cannot be achieved by a simple subtraction of the individual asymptotic solutions provided by Gomilko et al. [21] for the four singular corners, analytical solutions are required that simultaneously satisfy the discontinuous boundary condition for two corners which have a singular edge in common and which are separated by a finite distance. The solution of this problem, however, remains a formidable task for future analytical investigations.

Acknowledgments

We are very grateful to J.-L. Guermond for providing us with his quantitative data. The computing resources of the Center of Applied Space Technology and Microgravity (ZARM) of the University of Bremen are gratefully acknowledged. Part of this work has been carried out under DFG grant numbers KU896/8-1,2.

References

[1] A. Abouhamza, R. Pierre, 'A neutral stability curve for incompressible flows in a rectangular driven cavity', Math. Comput. Model. 38 (2003) 141–157.
[2] S. Albensoeder, H.C. Kuhlmann, H.J. Rath, 'Three-dimensional centrifugal-flow instabilities in the lid-driven cavity problem', Phys. Fluids 13 (2001) 121–135.
[3] F. Auteri, N. Parolini, L. Quartapelle, 'Numerical investigation on the stability of singular driven cavity flow', J. Comput. Phys. 183 (2002) 1–25.
[4] F. Auteri, L. Quartapelle, L. Vigevano, 'Accurate ω–ψ spectral solution of the singular driven cavity problem', J. Comput. Phys. 180 (2002) 597–615.
[5] V. Babu, S.A. Korpela, 'Numerical solutions of the incompressible, three-dimensional Navier–Stokes equations', Comput. Fluids 23 (1994) 675–691.
[6] U.T. Bödewadt, 'Die Drehströmung über festem Grunde', Z. Angew. Math. Mech. 20 (1940) 241–253.
[7] O. Botella, Résolution numérique de problèmes de Navier–Stokes singuliers par une méthode de projection Tchebychev, PhD thesis, Université de Nice–Sophia Antipolis, 1998.
[8] O. Botella, R. Peyret, 'Benchmark spectral results on the lid-driven cavity flow', Comput. Fluids 27 (1998) 421–433.
[9] O. Botella, R. Peyret, 'Computing singular solutions of the Navier–Stokes equations with the Chebyshev-collocation method', Int. J. Numer. Meth. Fluids 36 (2001) 125–163.
[10] O.R. Burggraf, 'Analytical and numerical studies of the structure of steady separated flows', J. Fluid Mech. 24 (1966) 113–151.

[11] T.P. Chiang, W.H. Sheu, R.R. Hwang, 'Three-dimensional vortex dynamics in a shear-driven rectangular cavity', Int. J. Comput. Fluid Dyn. 8 (1997) 201–214.
[12] T.P. Chiang, W.H. Sheu, R.R. Hwang, 'Effect of Reynolds number on the eddy structure in a lid-driven cavity', Int. J. Num. Meth. Fluids 26 (1998) 557–579.
[13] A.B. Cortes, J.D. Miller, 'Numerical experiments with the lid-driven cavity flow problem', Comput. Fluids 23 (1994) 1005–1027.
[14] G. De Vahl Davis, G.D. Mallinson, 'An evaluation of upwind and central difference approximations by a study of recirculating flow', Comp. Fluids 4 (1976) 29–43.
[15] M. Deville, T.-H. Lê, Y. Morchoisne, Numerical simulation of 3-D incompressible unsteady viscous laminar flows, Vol. 36 of Notes on Numerical Fluid Mechanics, Vieweg, Braunschweig, 1992.
[16] Y. Ding, M. Kawahara, 'Linear stability of incompressible fluid flow in a cavity using finite element method', Int. J. Numer. Meth. Fluids 27 (1998) 139–157.
[17] Y. Ding, M. Kawahara, 'Three-dimensional linear stability analysis of incompressible viscous flows using the finite element method', Int. J. Numer. Meth. Fluids 31 (1999) 451–479.
[18] C.J. Freitas, R.L. Street, A.N. Findikakis, J.R. Koseff, 'Numerical simulation of three-dimensional flow in a cavity', Int. J. Numer. Meth. Fluids 5 (1985) 561–575.
[19] U. Ghia, K.N. Ghia, C.T. Shin, 'High-Re solutions for incompressible flow using the Navier–Stokes equations and a multigrid method', J. Comput. Phys. 48 (1982) 387–411.
[20] K. Goda, 'A multistep technique with implicit difference schemes for calculating two- or three-dimensional cavity flows', J. Comput. Phys. 30 (1979) 76–95.
[21] A.M. Gomilko, V.S. Malyuga, V.V. Meleshko, 'On steady Stokes flow in a trihedral rectangular corner', J. Fluid Mech. 476 (2003) 159–177.
[22] J.W. Goodrich, K. Gustafson, K. Halasi, 'Hopf bifurcation in the driven cavity', J. Comput. Phys. 90 (1990) 219–261.
[23] J.-L. Guermond, C. Migeon, G. Pineau, L. Quartapelle, 'Start-up flows in a three-dimensional rectangular driven cavity of aspect ratio 1:1:2 at Re=1000', J. Fluid Mech. 450 (2002) 169–199.
[24] M.M. Gupta, R.P. Manohar, B. Noble, 'Nature of viscous flows near sharp corners', Comput. Fluids 9 (1981) 379–388.
[25] D.B. Haidvogel, T. Zang, 'The accurate solution of Poisson's equation by expansion in Chebyshev polynomials', J. Comput. Phys. 30 (1979) 167–180.
[26] P. Haldenwang, G. Labrosse, S. Abboudi, 'Chebyshev 3-D spectral and 2-D pseudospectral solvers for the Helmholtz equation', J. Comput. Phys. 55 (1984) 115–128.
[27] C. Hancock, E. Lewis, H.K. Moffatt, 'Effects of inertia in forced corner flows', J. Fluid Mech. 112 (1981) 315–327.
[28] W. Heinrichs, 'Splitting techniques for the unsteady stokes equations', SIAM J. Numer. Anal. 35 (1998) 1646–1662.
[29] R. Iwatsu, K. Ishii, K. Kuwahara, J.M. Hyun, 'Numerical simulation of three-dimensional flow structure in a driven cavity', Fluid Dyn. Res. 5 (1989) 173–189.
[30] J.R. Koseff, R.L. Street, 'On end wall effects in a lid-driven cavity flow', J. Fluids Eng. 106 (1984) 385–389.
[31] J.R. Koseff, R.L. Street, P.M. Gresho, C.D. Upson, J.A.C. Humphrey, W.-M. To, A three-dimensional lid-driven cavity flow: experiment and simulation, in: Proceedings of the 3rd International Conference on Numerical Methods in Laminar and Turbulent Flow, 1983, pp. 564–581.
[32] H.C. Ku, R.S. Hirsh, T.D. Taylor, 'A pseudospectral method for solution of the three-dimensional incompressible Navier–Stokes equations', J. Comput. Phys. 70 (1987) 439–462.
[33] H.C. Kuhlmann, M. Wanschura, H.J. Rath, 'Flow in two-sided lid-driven cavities: Non-uniqueness, instabilities, and cellular structures', J. Fluid Mech. 336 (1997) 267–299.
[34] E. Leriche, S. Gavrilakis, 'Direct numerical simulation of the flow in a lid-driven cubical cavity', Phys. Fluids 12 (2000) 1363–1376.
[35] H.K. Moffatt, 'Viscous and resistive eddies near a sharp corner', J. Fluid Mech. 18 (1964) 1–18.
[36] F. Pan, A. Acrivos, 'Steady flows in rectangular cavities', J. Fluid Mech. 28 (1967) 643–655.
[37] R. Peyret, Spectral methods for incompressible viscous flow, Applied Mathematical Science 148, Springer, New York, 2002.
[38] T.N. Phillips, G.W. Roberts, 'The treatment of spurious pressure modes in spectral incompressible flow calculations', J. Comput. Phys. 105 (1993) 150–164.
[39] E.M. Rønquist, Optimal spectral element methods for the unsteady three-dimensional incompressible Navier–Stokes equations, PhD thesis, Massachusetts Institute of Technology, 1998.
[40] R. Schreiber, H.B. Keller, 'Driven cavity flows by efficient numerical techniques', J. Comput. Phys. 49 (1983) 310–333.
[41] W.W. Schultz, N.Y. Lee, J.P. Boyd, 'Chebyshev pseudospectral method of viscous flows with corner singularities', J. Sci. Comput. 4 (1989) 1–24.
[42] P.N. Shankar, M.D. Deshpande, 'Fluid mechanics in the driven cavity', Annu. Rev. Fluid Mech. 32 (2000) 93–136.
[43] V. Shatrov, G. Mutschke, G. Gerbeth, 'Three-dimensional linear stability analysis of lid-driven magnetohydrodynamic cavity flow', Phys. Fluids 15 (2003) 2141–2151.
[44] J. Shen, 'Hopf bifurcation of the unsteady regularized driven cavity flow', J. Comput. Phys. 95 (1991) 228–245.
[45] T.W.H. Sheu, S.F. Tsai, 'Flow topology in a steady three-dimensional lid-driven cavity', Comput. Fluids 31 (2002) 911–934.

[46] Y. Spasov, J. Herrero, F.X. Grau, F. Giralt, 'Linear stability analysis and numerical calculations of the lid-driven flow in a toroidally shaped cavity', Phys. Fluids 15 (2003) 134–146.
[47] G.I. Taylor, On scraping viscous fluid from a plane surface, in: G.K. Batchelor (Ed.), The Scientific Papers of Sir Geoffrey Ingram Taylor, Vol. IV: Mechanics of Fluids – Miscellaneous Papers, Cambridge University Press, 1971, Cambridge, UK, 1962, pp. 410–413.
[48] M.M.T. Wang, T.W.H. Sheu, 'An element-by-element BICGSTAB iterative method for three-dimensional steady Navier–Stokes equations', J. Comp. Appl. Math. 79 (1997) 147–165.